Article | Received 3 November 2025; Revised 12 February 2026; Accepted 3 March 2026; Published 13 March 2026
https://doi.org/10.55092/sc20260004

Mechanical properties of Afghan vault integral structures based on simulated lunar soil

Qian Zhang[1], Huifang Chen[1], Jingyao Zhang[2], Yao Qu[3], SeungDeog Kim[1], Xuening Jiang[1], Jian Feng[1] and Jianguo Cai[1,*]

[1] Key Laboratory of C & PC Structures of Ministry of Education, National Prestress Engineering Research Center, Southeast University, Nanjing 211189, China
[2] Department of Architecture & Architectural Engineering, Kyoto University, Kyoto 615-8540, Japan
[3] CUCDE Environmental Technology Co.,Ltd., Beijing 100032, China

* Corresponding author; E-mail: j.cai@seu.edu.cn.

Highlights:

- Standardized specimen sizes were determined based on similar materials analysis.
- Systematic sintering experiments were conducted for the optimal test conditions.
- A self-locking Afghan vault structure was designed based on mortarless masonry.
- Parametrical analysis was developed under both static and dynamic lunar loads.

Abstract: *In-situ* construction technology refers to the direct use of indigenous resources of celestial bodies for construction and production activities in space exploration activities. Focusing on *in-situ* construction technology aims to improve the sustainability and cost efficiency of lunar missions by utilizing lunar indigenous resources. The research methodology involved sintering experiments using simulated lunar soil, where cubic specimens (40 mm × 40 mm × 40 mm) were prepared based on material similarity analysis. Based on differences in pressure and temperature, three distinct sintering conditions were designed for the experiments. The experimental results yielded essential material properties, including density, compressive strength, and shrinkage rate. Based on these mechanical properties and the characteristics of mortarless masonry, a self-locking Afghan vault structure was developed. Designed as an external shielding shell to protect internal inflatable habitats from radiation and meteorites, this structure functions under unpressurized conditions. Finite element analysis was employed to develop a parametric model of the Afghan vault structure, enabling comprehensive evaluation of its mechanical properties under both static and dynamic loading conditions. The study specifically analyzed the optimal construction angles under two different loading conditions: self-weight load and typical seismic load. Analysis revealed that structural stability was optimized at inclination angles of $\alpha = 30°$ and $\theta = 80°$ for these respective conditions. These research advancements have laid a theoretical foundation for the practical application of Afghan vault structures in lunar construction engineering.

Keywords: *in-situ* construction; simulated lunar soil; Afghan vault structure; high temperature sintering; Mortarless masonry

1. Introduction

As the nearest natural satellite to the Earth, the Moon has long been regarded as an important target for human space exploration and space resource utilization [1,2]. Recent advancements in international lunar exploration initiatives, notably NASA's Artemis Program [3] and the collaborative International Lunar Research Station (ILRS) project by China and Russia [4,5], have significantly accelerated lunar exploration efforts. This momentum is further reinforced by active participation from other space agencies, including those of Europe, Japan, South Korea, and India [6–8]. Within this context, the development of sustainable lunar base has emerged as a critical objective in contemporary space exploration strategies [9,10]. Construction of a lunar base requires substantial material resources. Given the prohibitive costs associated with Earth-Moon transportation, *in-situ* resource utilization (ISRU) has become an essential technological approach [11]. This strategy offers a sustainable pathway for lunar development by minimizing reliance on terrestrial materials, thereby addressing both economic and logistical challenges in extraterrestrial construction.

Various structural concepts have been proposed for lunar base construction, including rigid structures, deployable systems, inflatable modules, subsurface lava tube habitats, and hybrid configurations [12–16]. Inflatable structures are advantageous in terms of transportation, storage, construction, and reliability [13]. Rigid structures are resistant to meteorite particle impacts and have greater stability than inflatable structures, but they are inflexible and heavy, making them cost-ineffective [17]. Lava tube structures are located below the surface and offer better safety and reliability [14]. Hybrid structure designs can combine the advantages of multiple types of structures, e.g., combining the safety of rigid structures with the size and weight reduction advantages of inflatable structures [16]. Recent advancements in *in-situ* resource utilization (ISRU) have further expanded construction possibilities through innovative approaches, including 3D printing technologies, lunar soil-based concrete production, modular brick fabrication and lunar bag technology [18–20]. These ISRU-based construction methods not only substantially reduce Earth-launch material requirements by utilizing indigenous lunar resources but also enable more adaptable architectural solutions for extraterrestrial habitats. Current research initiatives include NASA's SinterHab project, which integrates deployable membrane structures with pre-fabricated rigid components and sintered regolith shells [20,21], and Foster + Partners' design incorporating inflatable modules with lunar soil shielding, utilizing D-Shape technology for on-site 3D printing of regolith bricks [22–24].

Contemporary international research on lunar *in-situ* construction technologies has identified five primary methodologies: stacking molding, sintering molding, fusion molding, compression molding, and bonding molding [25–31]. Stacking and compression molding rely on physical interlocking or mechanical compaction−simple and energy-efficient, but they produce low-strength, non-airtight components, limiting them to shielding walls rather than load-bearing structures. Bonding molding improves strength by adding chemical binders that cure the regolith, but the high cost of transporting these binders from Earth undermines the benefits of ISRU. In contrast, thermal methods like fusion and sintering bond regolith using heat alone, without Earth-sourced additives. Fusion fully melts the soil into a strong, glass-like solid, but it demands very high energy and precise temperature control. Sintering heats the material below its melting point, forming particle necks that offer better mechanical performance than compaction and lower energy use than fusion. For this reason, this study uses sintering to fabricate structural components. This process can be implemented either through pressureless *in-situ* sintering or enhanced with applied pressure within molds to improve material densification and mechanical properties [32]. Additionally, the bag-regolith technique, which uses flexible woven bags filled with lunar soil to form a structure, is also a method of forming lunar soil. This method offers significant advantages, including low energy consumption, minimal launch mass requirements, and compatibility with internal pressure-loading systems. Through optimized structural design and innovative engineering processes that meet load-bearing requirements, the bag-regolith technology has the potential to emerge as the most economically viable and operationally efficient construction method for lunar surface applications [20].

While numerous processing techniques have been developed for lunar regolith molding, the field currently lacks standardized specimen dimensions for mechanical property testing of lunar bricks, and existing designs for lunar surface construction exhibit limited structural diversity. This study systematically addressed the limitations of lunar *in-situ* construction by selecting appropriate dimensions for simulated lunar soil specimens through comparative analysis of material testing standards in Section 2. The specimens underwent mechanical property testing to derive material parameters for finite-element modeling. Focusing on mortarless masonry to address bonding material scarcity, a self-locking Afghan vault structure was designed as an unpressurized protective shell and parametrically modeled in Section 3. This design strategy avoids internal atmospheric loads, which is essential given the limited tensile capacity of the mortarless masonry. Consequently, its structural performance was analyzed under static loads and simulated lunar seismic activity, evaluating deformation patterns and stress-strain distributions to identify optimal construction angles. The conclusions are summarized in Section 4.

2. Simulated lunar soil specimens

2.1. Specimen size determination

The determination of appropriate specimen dimensions represents a critical step in measuring various material mechanical properties, as the specimen size significantly influences the test outcomes. Key factors affecting the size selection for simulated lunar soil specimens include the particle size distribution (both pre- and post-treatment), magnitude of mechanical properties, standardization practices, specimen fabrication complexity, and mechanical property stability [28]. To establish optimal specimen dimensions for simulated lunar soil, a comparative analysis with reference materials was conducted, leveraging established size-determination methodologies from related material studies.

Table 1 presents a comparative analysis of the particle size distribution (both pre- and post-molding), key mechanical properties, and specimen dimensions used in mechanical testing across different materials.

Table 1. Comparison of test specimen sizes for different material mechanical properties.

Material type	Particle size before treatment/mm	Particle size after treatment/mm	Mechanical performance indicators	Specimen size/mm
Metal [33]	Same particle size as after treatment	0.015–0.25(Grain after crystallization of metal)	Compressive strength 300–1000 MPa Elastic modulus around 200 GPa	Cylinders or square columns Compressive strength *L* = (2.5–3.5) *d* or (1–2) *d* Elastic modulus *L* = (5–8) *d*
Mortar [34]	Cement ≤ 0.9, Sand ≤ 5	Granule ≤ 5	Compressive strength 10–50 MPa Elastic modulus 30–50 GPa	Compressive strength 70.7 × 70.7 × 70.7 Elastic modulus 70.7 × 70.7 × (210–230)
Concrete [35]	Same particle size as after treatment	Split tensile test / Other tests ≤ 19.0 / ≤ 31.5 ≤ 37.5 / ≤ 37.5 - / ≤ 63.0	Compressive strength 15–50 MPa Elastic modulus 25–40 GPa	Minimum cross-section size 100 × 100 150 × 150 200 × 200
Bricks (red bricks, hollow bricks) [36]	≤ 3 (Brick factory screen size)		Compressive strength 10–30 MPa	Approximate size is about 100 × 100 × 100
Ceramics [37]	0.005–0.05 (Clay, will be processed again)	Dehydration, redox, Al_2O_3 and SiO_2 to form $Al_2O_3 \cdot SiO_2$ (vitrified porcelain)	Compressive strength 20–60 MPa	Cylinder diameter of common ceramic materials 20 mm, high 20 mm Cylinder diameter of coarse ceramic material 50 mm, high 50 mm
Simulated lunar soil (sintered) [22,23]	< 0.1 50%–52% 0.1–1 48%–50% > 1 0.5%–1.0%		Compressive strength around 50 MPa	-

The data reveals a correlation between particle size and specimen dimensions, demonstrating a positive proportionality. The pretreatment particle size ranges are 0.9–5 mm for mortar and 0.005–0.05 mm for ceramic materials, while simulated lunar regolith particles predominantly measure approximately 1 mm [38,39]. This intermediate particle size distribution suggests that appropriate specimen dimensions for simulated lunar soil should fall between those established for mortar and ceramic materials, that is, the side of the 70 mm cube and the diameter of 20 mm diameter cylindrical samples. To further validate the rigor of this selection, the ratio of specimen size (L) to the maximum particle size (d_{max}) was evaluated to ensure material representativeness. As shown in Table 1, the L/d max ratios for standard mortar and concrete specimens are approximately 14 and 3–5, respectively. For the CUG-1A simulant with a maximum particle size of approximately 1 mm, the selected 40 mm cubic specimen yields an L/d max ratio of 40. This ratio is substantially higher than those of the reference materials in Table 1, confirming that the 40 mm dimension is sufficient to eliminate boundary effects and provide stable, representative mechanical properties. Considering the practical testing constraints, a cubic specimen size of 40 mm × 40 mm × 40 mm was selected for this study.

2.2. Sintering test

The simulated lunar regolith material used in this study, CUG-1A, was sourced from the Qian Xuesen Space Technology Laboratory. To evaluate its geological representativeness, the chemical composition of CUG-1A is compared with the average composition of lunar regolith samples returned from the Apollo missions, as presented in Table 2. The comparative data demonstrates that CUG-1A exhibits a high degree of similarity to the Apollo 14 samples, which were collected from a highland region, thereby positioning it as a representative simulant for lunar highland regions [40]. This specific correlation ensures the reliability of using CUG-1A to simulate construction activities in lunar highland environments. Particle size distribution analysis revealed the following gradation: > 0.9 mm (5%), 0.2–0.9 mm (15%), 0.15–0.20 mm (20%), 0.074–0.15 mm (30%), and < 0.074 mm (30%) [41]. The elemental composition of CUG-1A is detailed in Table 2, with SiO_2 as its primary component, accounting for 48.32% by mass.

The experimental procedure, as illustrated in Figure 1a, commenced with the preparation of simulated lunar soil specimens. The lunar soil was initially placed in a mold and subjected to vibration compaction, followed by pressurization at 1.6 MPa using a pressure-testing apparatus to form specimens measuring 50.0 × 50.0 × 75.0 mm^3. The specimens were then sintered in a muffle furnace under varying conditions, and the pressure was determined by the specific sintering conditions. Subsequently, the sintered specimens were demolded and precisely cut to standardized dimensions of 40 mm × 40 mm × 40 mm using a waterjet cutting machine. Following a drying process, the specimens were subjected to compressive performance evaluation using a compressive-flexural testing machine.

Table 2. Chemical Composition of Apollo 14 and CUG-1A Regolith. (w_B/%) [40,41].

Samples	SiO_2	Al_2O_3	FeO_T	CaO	MgO	TiO_2	K_2O	P_2O_5	other
Apollo14	48.10	17.40	10.40	10.70	9.40	1.70	0.55	0.51	1.24
CUG-1A	48.32	16.01	12.50	7.39	6.95	2.38	2.12	0.54	3.79

Considering the high-temperature requirements of the sintering experiments, material reactivity at test temperatures, and mold fabrication costs, 310s stainless steel was selected for mold construction. The mold design, illustrated in Figure 1b, incorporates a separable liner with an internal cross-section of 50 mm × 50 mm to accommodate material shrinkage while maintaining specimen integrity during the sintering process.

Both the preliminary sintering experiments and formal tests on simulated lunar soil specimens were conducted under identical pressure conditions. The specimens, constrained within the mold, were subjected to a pressure of 4 kN (equivalent to 1.6 MPa) prior to sintering, as illustrated in Figure 1c. For the preliminary experiments, a temperature range of 850 ℃ to 1100 ℃ was employed with a controlled heating rate of 8 ℃/min [42,43]. After reaching the target temperature, the specimens were maintained at the designated temperature for 1 hour. Complete specimen formation was achieved at both 1050 ℃ and 1100 ℃, as demonstrated in Figure 1d. Based on the preliminary sintering results, three distinct experimental conditions were selected for further investigation: (1) 1050 ℃ with constraint but without applied pressure, (2) 1100 ℃ with constraint but without applied pressure, and (3) 1050 ℃ with both constraint and applied pressure.

The specimens sintered under different conditions were systematically designated as follows: “1050-n” and “1100-n” for those processed under unpressurized conditions, and “1050-Y-n” for the specimen sintered under pressurized conditions. To ensure experimental reliability, four to five replicates were prepared for each sintering condition. Following the quality assessment, three specimens exhibiting optimal structural integrity with minimal surface cracks were selected from each group for mechanical property testing after being precisely cut to the target dimensions. A representative sample of the sintered specimens is presented in Figure 1e.

To achieve the specified dimensions of the simulated lunar soil specimens, sanding and smoothing process was required prior to waterjet cutting. However, a proportion of specimens, particularly those sintered at 1050 ℃ and 1100 ℃ under unpressurized conditions, fractured during the sanding process, rendering them unsuitable for further testing. In contrast, the specimens sintered under pressurized conditions at 1050 ℃ demonstrated superior structural integrity, exhibiting minimal ring cracks due to the beneficial effects of pressure during sintering. This pressure application resulted in higher quality sintered specimens. Figure 1f illustrates representative specimens following the waterjet cutting process.

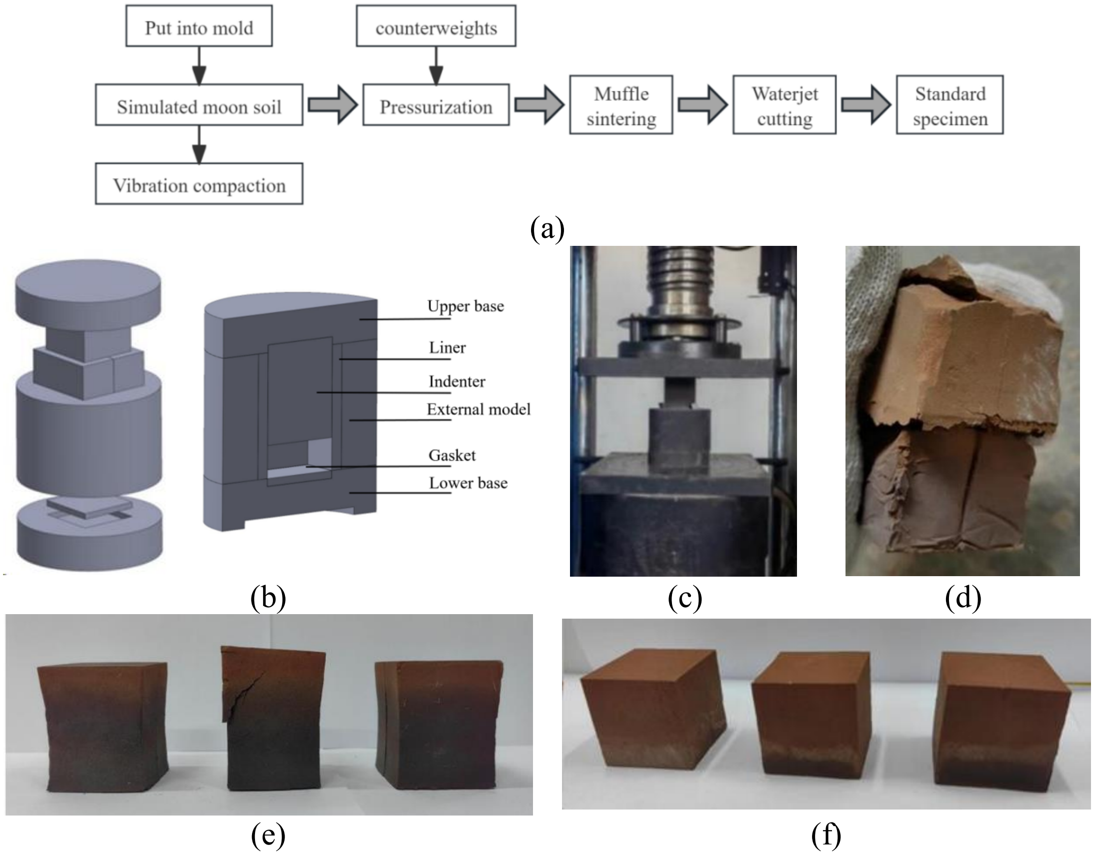

Figure 1. Test procedure and specimens. **(a)** Specimen production process; **(b)** Mold; **(c)** Pressurization; **(d)** Specimen; **(e)** Sintered specimens; **(f)** Standard specimens.

2.3. Test results

Sintered simulated lunar soil specimens, serving as fundamental components for *in situ* lunar surface construction, require comprehensive performance evaluation through parameters analogous to those used for terrestrial ceramics and red bricks. These evaluation metrics include density, compressive strength, compressive stress-strain characteristics, elastic modulus, and Poisson's ratio. Additionally, post-sintering dimensional shrinkage is a critical performance parameter in the evaluation process.

The sintering experiments of simulated lunar soil specimens revealed distinct morphological characteristics under different conditions. Specimens sintered at 1050 ℃ exhibited annular cracks measuring 1–1.5 mm in width, located 13–24 mm from the upper edge, accompanied by lower section shrinkage and minimal color variation. In contrast, the specimens processed at 1100 ℃ demonstrated smaller annular cracks in the upper region, more pronounced longitudinal cracks, and significant bulging in the lower section, with a notable color transformation from brick-red to dark grey, accompanied by substantial dimensional changes in the bulged areas. The 1050-Y series specimens, sintered under pressure, displayed superior mechanical properties characterized by reduced crack formation, uniform coloration, and lower shrinkage rates. However, specimen 1050-Y-4 exhibited inferior sintering quality, manifested through increased crack density and significant dimensional variations. This degradation is primarily attributed to non-uniform pressurization during the fabrication process. Specifically, stress concentrations occurred at the seams of the mold liner, leading to the formation of substantial longitudinal cracks and localized defects during sintering.

The shrinkage characteristics of the simulated lunar soil are presented in Figure 2a. The 1050-n specimens exhibit average transverse and longitudinal shrinkage rates of 8.1% and 5.7%, respectively, with greater contraction observed in the transverse direction. Elevated sintering temperatures significantly increase shrinkage, as demonstrated by the 1100-n specimens, which show average transverse and longitudinal shrinkage rates of 14.2% and 18.3%, respectively, with longitudinal shrinkage exceeding transverse values. The 1050-Y-n specimens display intermediate behavior, with average transverse shrinkage of 9.1% and longitudinal shrinkage of 15.1%, exhibiting the most pronounced anisotropy among the three groups.

These results indicate that both elevated temperatures and pressurization contribute to increased shrinkage in simulated lunar soil, with temperature variations exerting a more pronounced influence on specimen characteristics. Morphological analysis of the sintered specimens suggests that applied pressure during sintering enhances the compaction of simulated lunar soil, effectively reducing transverse crack formation and improving overall sintering quality.

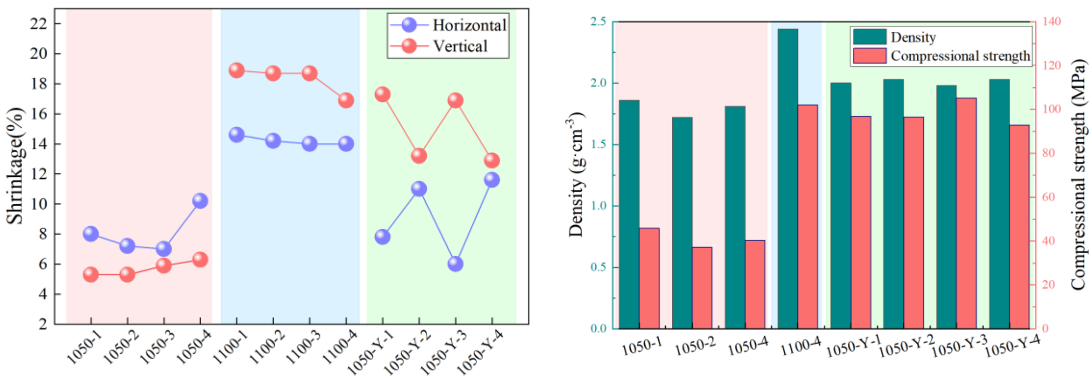

(a) (b)

Figure 2. Performance of sintered lunar soil specimens. **(a)** Specimen shrinkage; **(b)** Specimen density, compressive strength.

Figure 2b presents the density and compressive strength distributions of simulated lunar soil specimens through bar graphs. The 1050-n specimens exhibit an average density of 1.80 g/cm^3; while the 1100-4 specimen, under identical unpressurized conditions, demonstrates a significant increase in average density to 2.44 g/cm^3. Additionally, the average density of the 1050-Y-n specimens increases to 2.01 g/cm^3. These experimental results demonstrate that both elevated sintering temperatures and applied pressure significantly enhance material densification, with temperature exerting a more pronounced influence under the tested conditions.

The 1050-n specimens exhibit an average compressive strength of 41.07 MPa, while the 1100-4 specimen demonstrates significantly higher strength, averaging 101.87 MPa. Similarly, the average compressive strength of the 1050-Y-n specimens is 97.85 MPa. Notably, the compressive strength achieved through pressurized sintering at 1050 ℃ is comparable to that obtained via unpressurized sintering at 1100 ℃. These experimental results demonstrate that both elevated sintering temperatures and applied pressure significantly enhance the mechanical strength of the sintered specimens.

The stress-strain characteristics of simulated lunar soil specimens are presented in Figure 3. Under unpressurized sintering conditions at 1050 ℃, the specimens demonstrate a linear stress-strain relationship until reaching their compressive limit, at which point sudden failure occurs, exhibiting an average compressive strength of 41.07 MPa and an elastic modulus of 13.48 GPa. In contrast, the 1050-Y-n specimens display distinct mechanical behavior, characterized by less smooth stress-strain curves and a significantly higher stress limit of approximately 90 MPa. These pressurized specimens exhibit brittle failure with an average elastic modulus of 31.25 GPa, indicating that applied pressure during sintering enhances the material's elastic modulus while reducing longitudinal deformation under compressive loading.

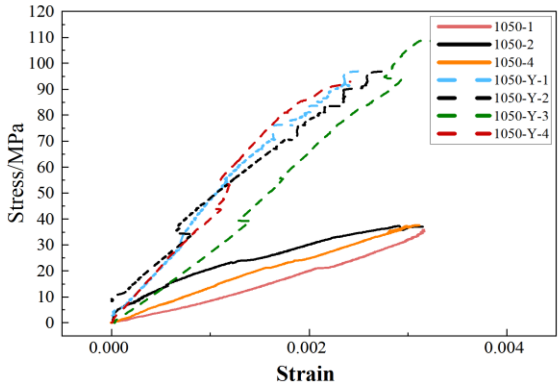

Figure 3. Stress-strain curves of simulated sintered lunar soil specimens.

3. Mechanical study of Afghan vault integral structure

3.1. Structural design

Mortarless masonry construction emerges as a preferred solution for lunar surface construction, effectively addressing the challenge of bonding material scarcity. Drawing inspiration from the vernacular architecture of Afghanistan, this study adopts the Afghan vault configuration. As illustrated in Figure 4a, this system is uniquely characterized by its woodless construction technique [44]. Unlike conventional radial arches that necessitate timber centering, the Afghan vault enables construction without the need for formwork. Consequently, this structural system is highly suitable for lunar environments where auxiliary construction resources are limited. The Afghan vault, a self-locking structural system, employs a unique construction methodology: initiating from the base edges or corners of opposing squares, bricks are systematically stacked inward at predetermined inclination angles. The structural integrity is achieved through an interlocking mechanism, where bricks from opposing sides intersect and stagger, culminating in a stable, mortar-free configuration upon placement of the final keystone brick. This design philosophy is the key enabler for mortarless masonry. By ensuring that the stresses within the structure remain compressive, the need for mortar, which traditionally serves to bind bricks and resist tensile forces, is eliminated. The sintered bricks are essentially pushed together by the geometry of the vault, relying on their own compressive strength and the interlocking nature of their placement to maintain structural integrity.

The Afghan vault structure composed of sintered lunar soil bricks inherently provides the necessary radiation and meteorite protection, eliminating the need for an additional regolith covering layer. Therefore, the self-weight analyzed in this study represents the primary static load. Since the structure functions as a protective cover over a pressurized core, it does not bear internal atmospheric loads. For computational efficiency in modeling and finite element analysis, this study adopts the Afghan vault configuration illustrates in Figure 4b, with the detailed construction process schematically presents in Figure 4c.

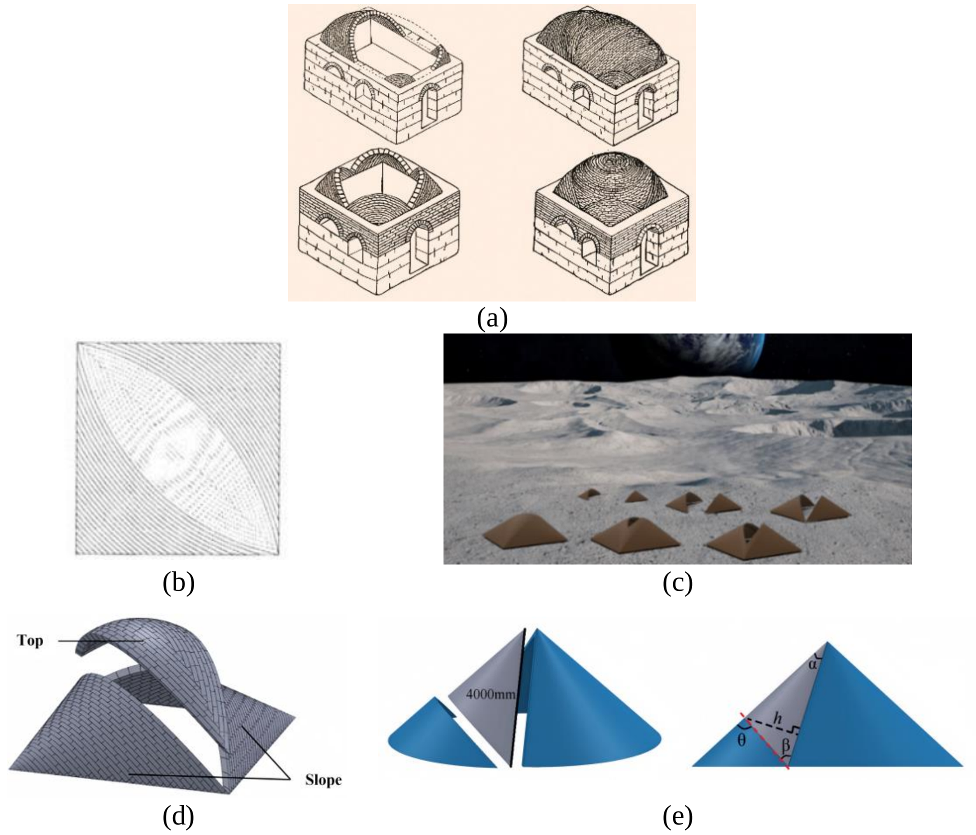

Figure 4. Afghan vault. **(a)** Traditional Afghan vaulting method; **(b)** Type of construction; **(c)** Construction process; **(d)** Components; **(e)** Geometric sketch.

The Afghan vault structure comprises three primary components: bilateral inclined slopes converging inward at specific angles, and a central keystone section that facilitates structural conjunction. Based on practical construction considerations [45,46], the base dimension of the vault was established at 4000 mm. The wall thickness, corresponding to the width of individual construction bricks, was modeled at 115 mm, as illustrated in Figure 4d to clarify the structural composition, the correlation between the material testing and the structural design was established. The 40 × 40 × 40 mm cubic specimens (Section 2) were used to determine the constitutive material properties, which were then assigned to the full-scale bricks in the Afghan vault model. The individual bricks were designed with standard dimensions of 240 × 115 × 53 mm. Regarding the construction parameters, a mortarless dry-stacking method was adopted with a negligible gap (assumed to be 0 mm) to simulate tight contact. The detailed construction sequence of the Afghan vault is illustrated in Figure 5. A strict 1/2 staggered overlap (running bond) was implemented between adjacent layers. This construction design significantly enhances the self-locking performance: the staggered overlap ensures the continuity of shear transfer paths and prevents the formation of through-vertical cracks, while the specific inclination angles convert the gravitational component of the bricks into normal pressure on the contact surfaces, thereby maximizing static friction to resist sliding and maintain structural equilibrium.

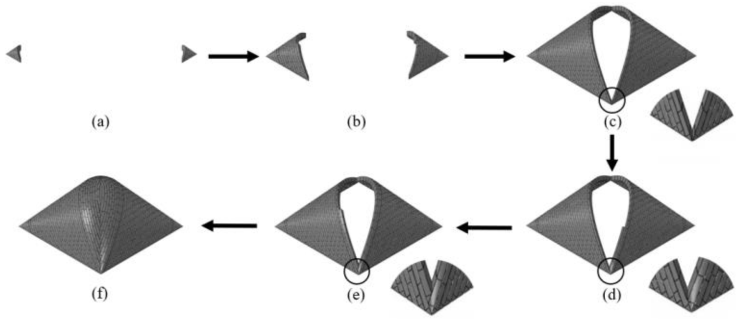

Figure 5. Construction process of the Afghan vault.

Given the absence of explicit geometric curves in traditional Afghan vault construction, the modeling process incorporates simplifications to facilitate computational analysis. The bilateral slopes are represented as truncated conical sections, formed by intersecting a conical surface with a cutting plane, as illustrated in Figure 4e. The blue regions depict the removed conical surfaces post-intersection, while the gray sections define three critical angular parameters: slope angle (α), ground angle (β), and their composite angle ($\theta = \alpha + \beta$). The top section of the Afghan vault is generated through the rotational transformation of the red dashed cross-section about the axis connecting the vertices of two β angles. The structural height parameters include the slope apex height (h), and the total vault height (H).

The finite element analysis primarily examines the stress distribution patterns, structural deformation characteristics, and geometric parametric influences on the mechanical performance of Afghan vault models under both static loading and moonquake conditions. Nine distinct parametric configurations were systematically designed, employing a standardized nomenclature system (SPα-θ) for model identification. The detailed geometric parameters corresponding to each model configuration are presented in Table 3. The selection of these geometric parameter ranges is grounded in physical constructability constraints specific to mortarless masonry. Specifically, the inclination angle α is strictly limited by the static friction coefficient between the sintered bricks. Angles exceeding 40 °would risk immediate sliding failure during the stacking process without binders, while angles below 20 °reduce spatial efficiency. These ranges ensure the validity of the self-locking mechanism during the critical construction phase.

Table 3. Finite element model parameters of Afghan vault.

Number	α	β	θ	Height at the top of the slope h/mm	Total height H/mm
SP20-70	20°	50°	70°	788.41	1029.46
SP20-80	20°	60°	80°	850.69	982.3
SP20-90	20°	70°	90°	909.02	967.38
SP30-70	30°	40°	70°	967.38	1504.97
SP30-80	30°	50°	80°	1100.06	1436.02
SP30-90	30°	60°	90°	1224.73	1414.21
SP40-70	40°	30°	70°	967.35	1934.76
SP40-80	40°	40°	80°	1186.65	1846.12
SP40-90	40°	50°	90°	1392.69	1818.08

3.2. Finite element modeling

The primary objective of the modeling is to investigate the overall stress distribution within the finite element model and determine optimal model parameters. The Afghan vault entity model is constructed using SolidWorks, with each component built separately and then assembled. The assembled model is imported into ABAQUS for finite element simulation analysis using the Standard module. The component type is defined as a 3D deformable body. To simplify the contact settings of the finite element model and avoid unnecessary computational resource consumption, the model is not divided into block entities. Instead, the three parts of the Afghan vault are directly bound together face-to-face after modeling. This tied contact approach serves as a first-level approximation for evaluating the structure's global behavior. The validity of this monolithic model is grounded in the vault's compression-dominant state, which is confirmed by two key points. First, the subsequent Finite Element Analysis (FEA) results reveal negligible tensile stresses. Second, a separate theoretical equilibrium analysis verifies the frictional self-locking mechanism of the mortarless joints. This analytical check confirms that the geometric configuration satisfies the stability criterion $\mu \geq \tan\beta \cdot \cos\gamma$ (assuming a friction coefficient $\mu = 0.6$), ensuring the joints remain stable under gravitational loads. Consequently, these physical justifications confirm that the continuous model effectively captures the macroscopic performance of the structure. The bottom of the model is then subjected to a fully fixed constraint. Given the irregular three-dimensional geometry of the model, a 10-node quadratic tetrahedral element (C3D10) is selected.

The material constitutive model for the Afghan vault is based on the simplified mechanical properties of simulated lunar soil sintered at 1050 ℃ under pressurized conditions. The material properties are as follows: density $\rho = 2.0$ g/cm³; elastic modulus $E = 31.25$ GPa, Poisson ratio $\upsilon = 0.30$, and compressive strength $\sigma_{bc} = 97.85$ MPa. The material constitutive behavior is modeled as linear elastic. This approach is supported by the experimental stress-strain curves (Figure 3), which demonstrate a linear response up to the point of brittle failure. Furthermore, as the finite element analysis indicates that the structure's operational stresses are significantly lower than the material's failure threshold, the structure remains well within the elastic region, making the linear elastic model appropriate for this design phase.

3.3. Static analysis

Given that the gravitational acceleration on the Moon is only 1/6 of that on Earth, a value of g = 1.633 m/s^2 is adopted for the self-weight analysis.

(1) Vertical displacement

Figure 6 presents the vertical displacement distribution of the parametric model under self-weight conditions, demonstrating that significant displacement values are predominantly localized in the upper region of the Afghan vault. For $\theta = 70°$, the maximum vertical displacements corresponding to slope angles α of 20°, 30°, and 40° are 1.06 mm, 0.65 mm, and 0.58 mm, respectively. These displacements represent 0.10%, 0.043%, and 0.030% of the total height of the Afghan vault. Similarly, for $\theta = 80°$, the maximum vertical displacements for slope angles α of 20°, 30°, and 40° are 0.96 mm, 0.66 mm, and 0.58 mm, accounting for 0.097%, 0.046%, and 0.031% of the total height, respectively. When $\theta = 90°$, the maximum vertical displacements for slope angles α of 20°, 30°, and 40° are 0.93 mm, 0.69 mm, and 0.60 mm, representing 0.096%, 0.049%, and 0.033% of the total height, respectively.

The data indicates a consistent trend: as both θ and α increase, the maximum vertical displacement values and their proportions relative to the total height of the vault progressively decrease. These results imply that optimal structural design of the Afghan vault should incorporate relatively larger α and θ values within their respective feasible ranges.

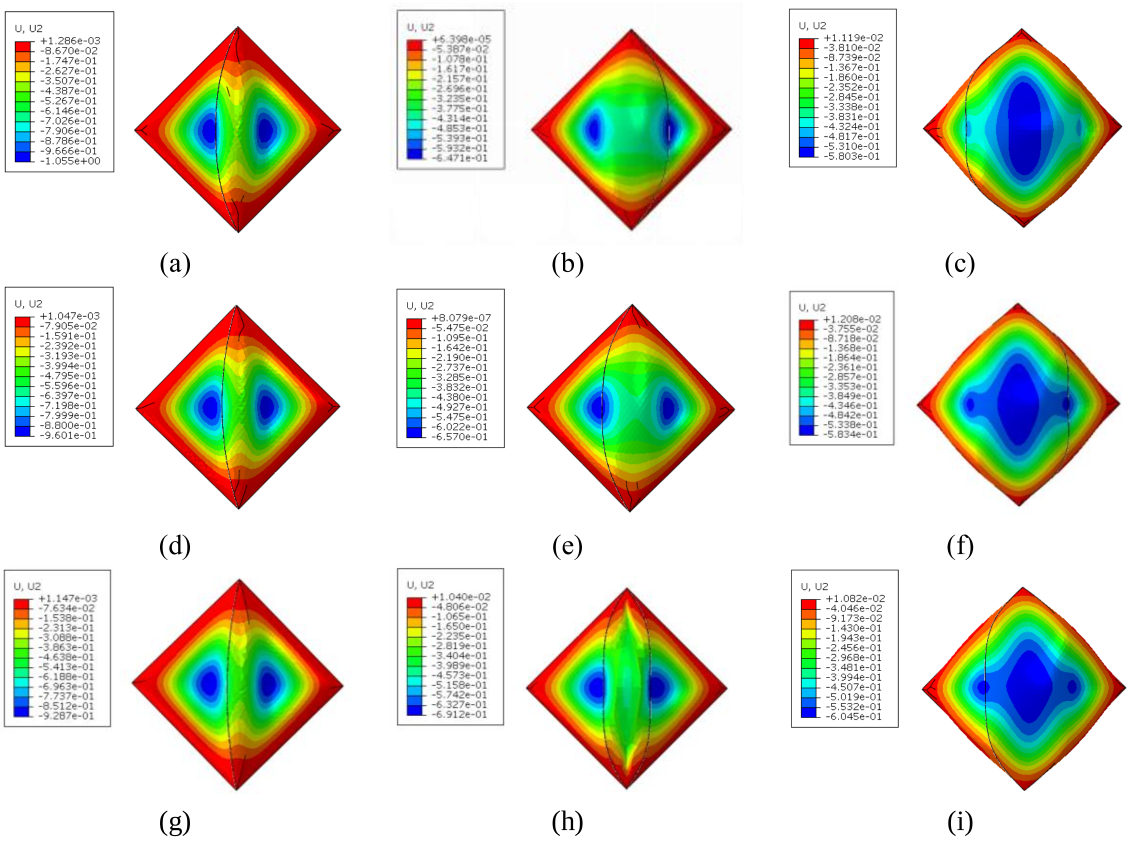

Figure 6. Vertical displacements of models with different parameters under self-weight(mm). **(a)** SP20-70; **(b)** SP30-70; **(c)** SP40-70; **(d)** SP20-80; **(e)** SP30-80; **(f)** SP40-80; **(g)** SP20-90; **(h)** SP30-90; **(i)** SP40-90.

(2) Stress distribution

Figure 7 illustrates the overall stress distribution of the Afghan vault for varying angles of α and θ. The analysis reveals that stress concentrations predominantly occur on the left and right sides of the slope. At $\theta = 70°$, the maximum stresses corresponding to slope angles α of 20°, 30°, and 40° are 0.01473 MPa, 0.026 MPa, and 0.012 MPa, respectively. For $\theta = 80°$, the maximum stresses at the same slope angles are 0.013 MPa, 0.0093 MPa, and 0.0113 MPa, respectively. When $\theta = 90°$, the maximum stresses for slope angles α of 20°, 30°, and 40° are 0.013 MPa, 0.00931 MPa, and 0.011 MPa, respectively.

The results demonstrate distinct trends in stress behavior. For $\theta = 70°$ and $\theta = 80°$, the maximum stress decreases as α increases. However, at $\theta = 90°$, the maximum stress initially decreases and then increases with increasing α. Additionally, when $\alpha = 20°$, the maximum stress decreases initially and then increases with increasing θ. For $\alpha = 30°$ and $\alpha = 40°$, the maximum stress exhibits an inverse proportionality with θ. These findings indicate that the maximum stress of the Afghan vault model does not follow a purely positive or negative correlation with α and θ. Among the nine models analyzed, SP30-80 demonstrates superior mechanical properties, characterized by the smallest maximum stress. It is noteworthy that the maximum stresses across all configurations remain far below the compressive strength of the sintered lunar soil. This indicates that the Afghan vault is significantly over-designed for lunar gravity conditions, offering an extreme safety margin that ensures structural reliability even under unforeseen localized defects.

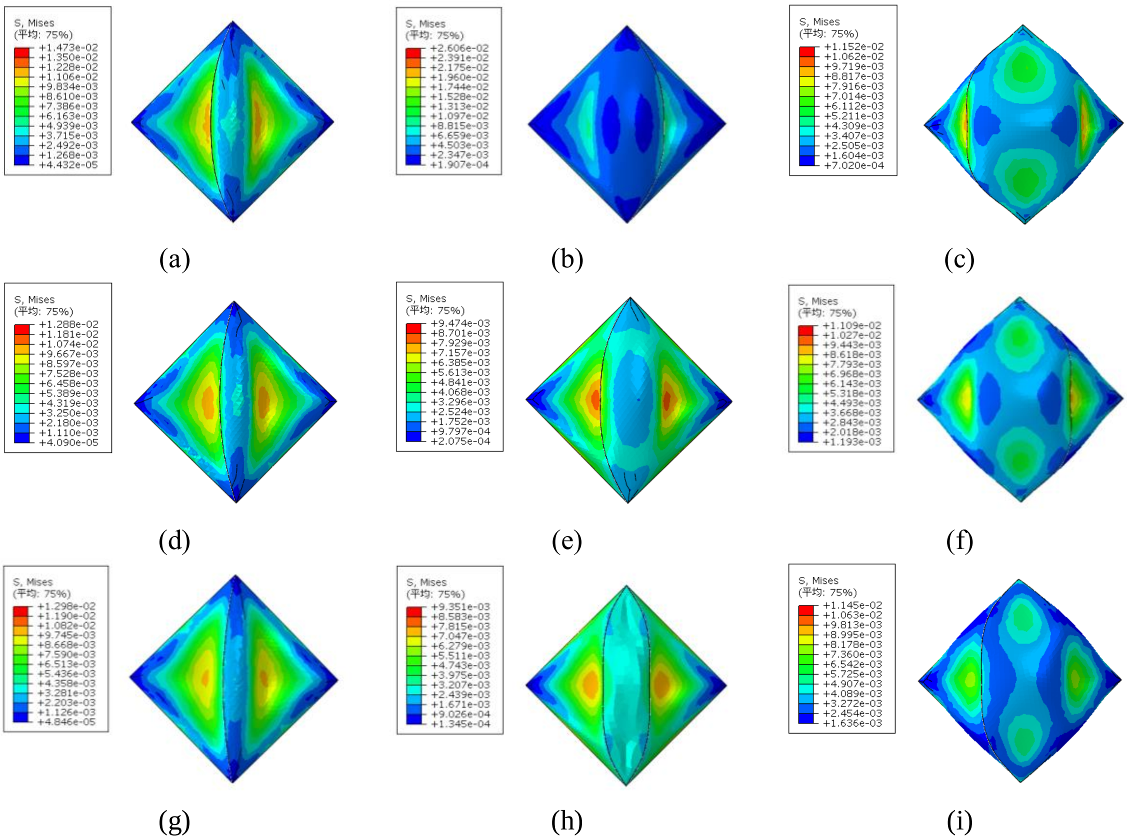

Figure 7. Stress distribution of models with different parameters under self-weight (MPa). **(a)** SP20-70; **(b)** SP30-70; **(c)** SP40-70; **(d)** SP20-80; **(e)** SP30-80; **(f)** SP40-80; **(g)** SP20-90; **(h)** SP30-90; **(i)** SP40-90.

(3) Tensile and compressive stresses

Table 4 summarizes the maximum tensile and compressive stresses for each modeled structure, along with their corresponding stress ratios. The results indicate that the maximum compressive stresses in the structures are significantly lower than the compressive strength of the simulated lunar soil sintered specimens. By optimizing the geometric parameters α and θ, the tensile stresses within the Afghan vault model are substantially reduced, resulting in a stress state dominated by compressive forces. For instance, the SP30-80 model exhibits the lowest maximum tensile stress of 0.0011 MPa among all configurations, with a tensile-to-compressive stress ratio of 0.104. This behavior aligns closely with the stress distribution observed in traditional Afghan vault construction, where structural stability is achieved through compressive forces between bricks, enabling the implementation of mortar-free masonry systems. Although the specific tensile strength of the simulated lunar soil was not characterized in this study, the maximum tensile stress observed in the finite element analysis is extremely low (only 0.0255 MPa). This value is several orders of magnitude lower than the measured compressive strength (97.85 MPa). Given that the structure is designed to be compression-dominant, such minute tensile stresses are negligible and fall well within the safety margins of sintered ceramic-like materials, indicating no risk of tensile failure.

Table 4. Maximum tensile and compressive stresses of models under self-weight.

Number	Maximum tensile stress/MPa	Maximum compressive stress/MPa	Stress ratio
SP20-70	0.0176	0.0203	0.867
SP20-80	0.0055	0.0147	0.374
SP20-90	0.0060	0.0178	0.227
SP30-70	0.0255	0.0320	0.797
SP30-80	0.0011	0.0106	0.104
SP30-90	0.0020	0.0105	0.190
SP40-70	0.0057	0.0170	0.335
SP40-80	0.0068	0.0166	0.410
SP40-90	0.0048	0.017	0.282

3.4. Dynamic performance analysis

3.4.1. Angle of the moonquake waves

The Chalfant Valley-02 wave is selected to simulate the moonquake effect, with a duration of 40 seconds. Although moonquakes on the lunar surface are typically of low magnitude [47], a conservative design strategy is essential given the high reliability requirements for inhabited lunar bases where structural repair is extremely difficult. Considering the strict safety requirements for lunar habitats and the necessity of exploring potential applications on other planetary bodies with varying seismic activities, a peak ground acceleration (PGA) of 0.2 g (corresponding to seismic intensity VIII) was selected. This intensity serves to simulate a rare but high-risk shallow moonquake scenario, thereby providing a reliable safety margin. The amplitude-adjusted acceleration time-history curve of the Chalfant Valley-02 wave is illustrated in Figure 8a.

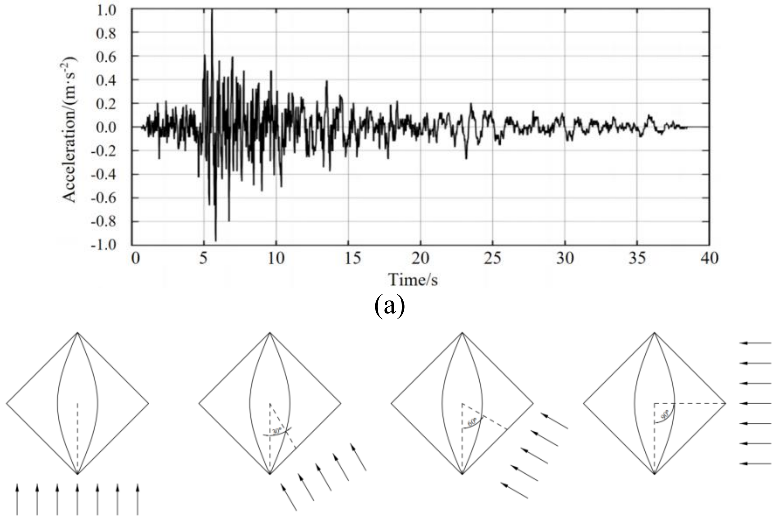

Figure 8. Moonquake wave. **(a)** Acceleration time-history course curve; **(b)** Direction of moonquake wave imposition.

To evaluate the dynamic response efficiently, a two-stage analysis was adopted. A dynamic time-course analysis was conducted on the Afghan vault model under combined loading conditions, including self-weight and seismic excitation from the Chalfant Valley-02 wave. In the first stage, four wave propagation angles

(0°, 30°, 60°, and 90°) relative to the x-axis were investigated. As illustrated in Figure 8b, these angles were applied to three representative configurations (SP20-80, SP30-80, and SP40-80) to identify the most critical loading direction while minimizing computational costs. In the second stage, the identified critical angle was applied to all nine parametric models to determine the optimal geometric configuration under seismic excitation.

(1) Vertical displacement

Figure 9 presents the deformation patterns of the three selected models (SP20-80, SP30-80, and SP40-80) under the moonquake wave with varying loading angles. The results reveal that models with different α values exhibit distinct deformation behaviors even under identical loading angles. Table 5 summarizes the maximum vertical displacements under different loading angles of the moonquake wave. The analysis reveals that the most unfavorable loading angles for the three models are 90°, 0°, and 30°, respectively. This suggests that there is no clear or consistent relationship between the maximum vertical displacement and the loading angle for a given model subjected to moonquake waves from different directions. Consequently, further investigation is necessary to evaluate the influence of moonquake waves at varying angles on the tensile stress index, with the aim of identifying the most critical loading scenario for structural stability.

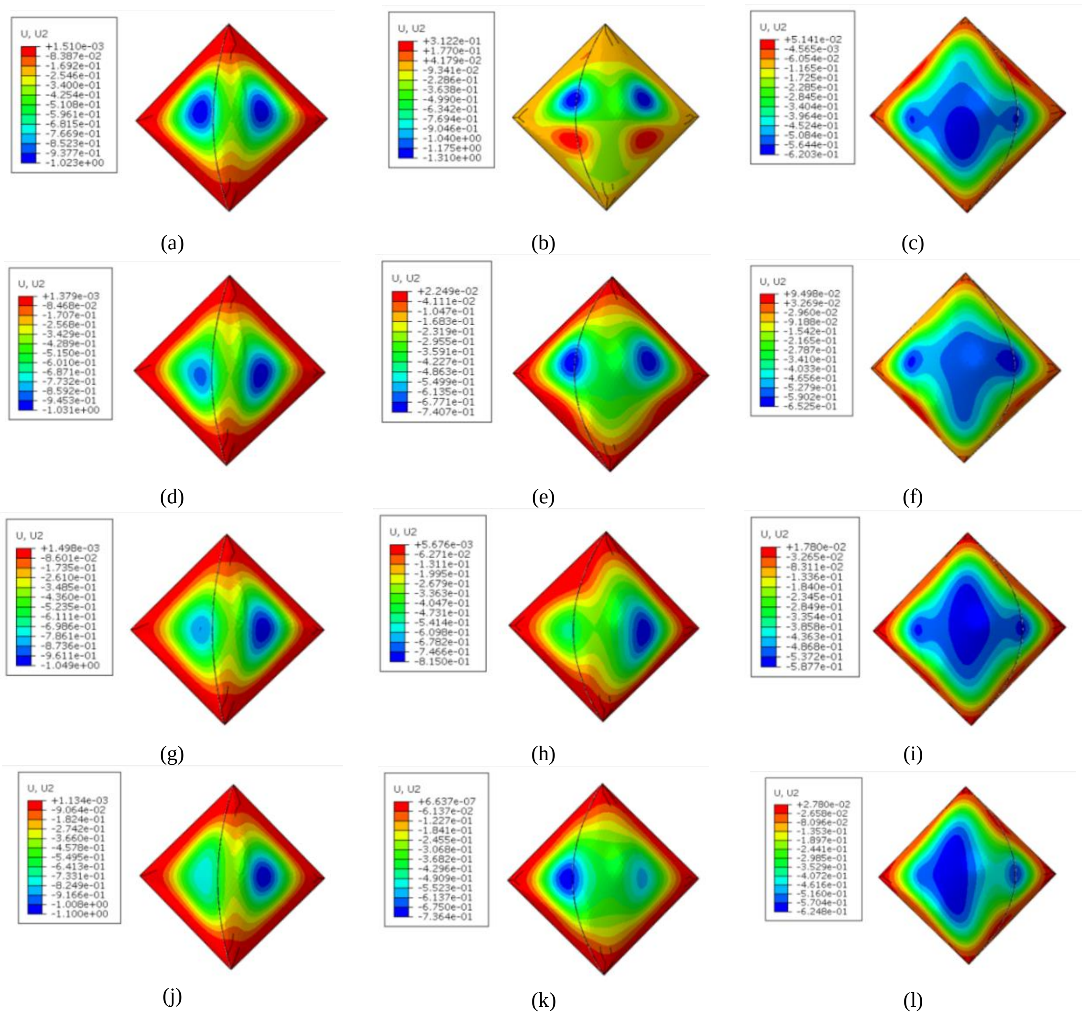

Figure 9. Vertical displacements at different moonquake wave loading angles (mm). **(a)**SP20-80, 0°; **(b)** SP30-80, 0°; **(c)** SP40-80, 0°; **(d)** SP20-80, 30°; **(e)** SP30-80, 30°; **(f)** SP40-80, 30°; **(g)** SP20-80, 60°; **(h)** SP30-80, 60°; **(i)** SP40-80, 60°; **(j)** SP20-80, 90°; **(k)** SP30-80, 90°; **(l)** SP40-80, 90°.

Table 5. Maximum vertical displacements for different moonquake wave loading angles.

Loading angle	SP20-80	SP30-80	SP40-80
0°	1.023	1.310	0.620
30°	1.031	0.741	0.653
60°	1.049	0.815	0.588
90°	1.100	0.736	0.625

(2) Tensile stress

Given that compressive stress has a relatively minor impact on the structural integrity of the Afghan vault, while tensile stress poses a more significant threat to its stability, the tensile stress distributions of the three selected models (SP20-80, SP30-80, and SP40-80) under varying loading angles of moonquake waves are presented in Figure 10. Table 6 summarizes the maximum tensile stresses under these conditions. A comparative analysis reveals that the maximum tensile stresses for the three models occur at a loading angle of 30°, measuring 0.0065 MPa, 0.0026 MPa, and 0.0105 MPa, respectively. These results indicate that a loading angle of 30° represents the most critical condition influencing the stability of the models. The failure mechanism is attributed to the asymmetry of the dynamic loading relative to the structure's geometry. Unlike 0° or 90° waves that align with the symmetry axes, the 30° oblique wave generates significant torsional effects and asymmetric shear stresses along the brick interfaces. This specific loading direction maximizes the disruption of the frictional self-locking mechanism, leading to the peak vertical displacements and tensile stresses observed. Consequently, subsequent dynamic time-course analyses focus on this loading angle to evaluate the structural response under the most unfavorable conditions.

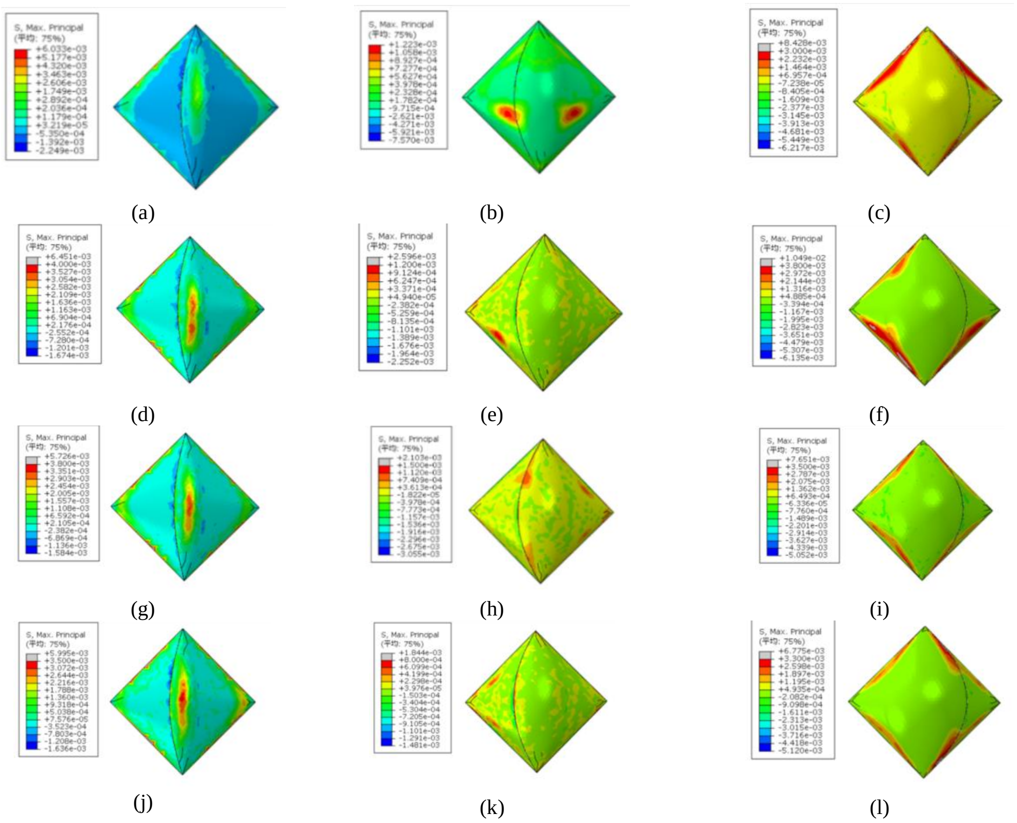

Figure 10. Tensile stress cloud at different loading angles of the moonquake wave (MPa). **(a)** SP20-80, 0°; **(b)** SP30-80, 0°; **(c)** SP40-80, 0°; **(d)** SP20-80, 30°; **(e)** SP30-80, 30°; **(f)** SP40-80, 30°; **(g)** SP20-80, 60°; **(h)** SP30-80, 60°; **(i)** SP40-80, 60°; **(j)** SP20-80, 90°; **(k)** SP30-80, 90°; **(l)** SP40-80, 90°.

Table 6 Maximum tensile stresses at different moonquake wave loading angles.

Maximum tensile stress/MPa	SP20-80	SP30-80	SP40-80
0 °	0.0060	0.0012	0.0084
30 °	0.0065	0.0026	0.0105
60 °	0.0057	0.0021	0.0077
90 °	0.0060	0.0018	0.0068

3.4.2. Dynamic performance analysis results

(1) Vertical displacement

Figure 11 illustrates the vertical displacements of models with varying geometric parameters under the moonquake wave loading angle of 30 °. The results indicate that the maximum vertical displacements of individual models exhibit inconsistent trends under seismic excitation, with no discernible pattern. Through comparative analysis, the SP30-80 model demonstrates the smallest range of vertical displacement variation among all configurations, with a maximum upward deformation of 0.022 mm and a maximum downward deformation of 0.741 mm. These findings indicate that the model with α = 30 ° and θ = 80 ° achieves optimal structural performance under lunar shock wave loading conditions.

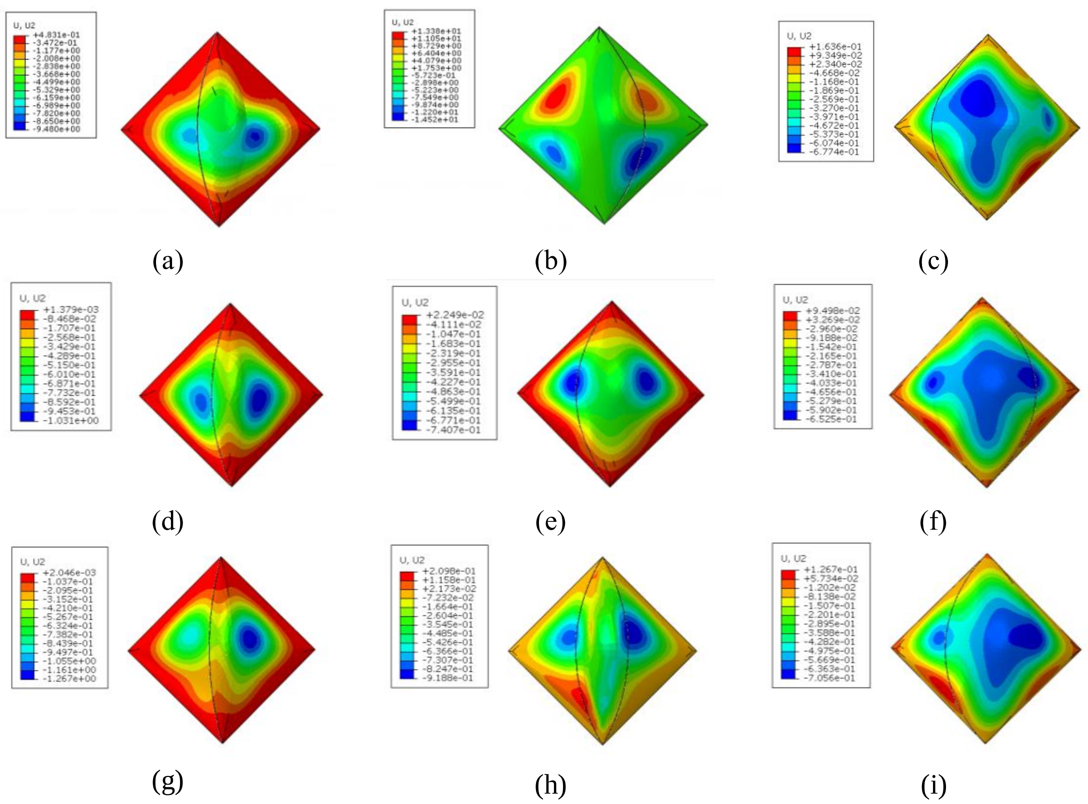

Figure 11. Vertical displacements of models with different parameters under the effect of moonquake waves (mm). **(a)** SP20-70; **(b)** SP30-70; **(c)** SP40-70; **(d)** SP20-80; **(e)** SP30-80; **(f)** SP40-80; **(g)** SP20-90; **(h)** SP30-90; **(i)** SP40-90.

(2) Tensile and compressive stresses

Table 7 presents the tensile and compressive stress distributions of models with varying geometric parameters under a 30 ° moonquake wave. The data indicate that the SP40-70 model experiences the highest compressive stress among all configurations, with a maximum value of 0.025 MPa. This stress level remains significantly below the compressive strength of sintered simulated lunar soil specimens processed at 1050 ℃ under applied pressure, confirming the structural adequacy of the Afghan vault configuration under compressive loading conditions. Given the critical influence of tensile stress on structural stability, particular attention is given to the maximum tensile stress values. The SP30-80 model demonstrates the lowest maximum tensile stress at 0.005 MPa, indicating optimal dynamic load-bearing performance when α = 30° and θ = 80°.

Table 7 Tensile and compressive stresses in models under the action of 30° moonquake waves.

Number	Maximum tensile stress/MPa	Maximum compressive stress/MPa	Tensile to compressive stress ratio
SP20-70	0.006	0.02	0.3
SP20-80	0.006	0.016	0.375
SP20-90	0.009	0.019	0.474
SP30-70	0.006	0.021	0.286
SP30-80	0.005	0.013	0.384
SP30-90	0.007	0.014	0.5
SP40-70	0.013	0.025	0.52
SP40-80	0.011	0.02	0.55
SP40-90	0.01	0.02	0.5

3.5. Discussion

The extremely low stress values obtained in the simulations (0.01–0.03 MPa), compared to the 97.85 MPa compressive strength of the sintered lunar soil, indicate a massive safety margin. In the context of lunar construction feasibility, this suggests that the Afghan vault is highly tolerant of potential material defects or inconsistencies in the sintering process. By serving as a protective cover over a pressurized core, the structure effectively shields internal habitats from radiation and meteorites, making it a robust candidate for early lunar base shielding. Compared to the rigid domes or radial arches mentioned in Introduction, which typically require complex formwork or temporary supports during construction, the Afghan vault's self-locking, mortarless design offers a significant advantage for *in-situ* resource utilization by eliminating the need for terrestrial-sourced auxiliary materials.

Furthermore, the identification of optimal construction angles (α = 30° and θ = 80°) provides critical geometric parameters for autonomous robotic systems. These angles can serve as the baseline for robotic path planning and block-laying sequences, ensuring structural stability is maintained throughout the construction process without human intervention. However, it is important to acknowledge the limitations of this study. The current finite element analysis employs simplified linear constitutive models and tied contact interfaces, which may not fully capture the complex frictional sliding behavior of mortarless masonry. Additionally, the lack of a physical scale model and the use of simplified seismic waves necessitate future experimental validation to confirm the structural response under more complex, non-linear loading scenarios.

4. Conclusions

This study investigates the application of *in-situ* construction techniques for lunar surface buildings through an integrated approach combining material characterization, structural design, and numerical analysis. The research methodology commenced with sintering experiments on simulated lunar soil to determine its fundamental mechanical properties, which were subsequently implemented in the design of a mortarless masonry structure based on the Afghan Vault configuration. These material properties were then incorporated into finite element parametric modeling, enabling comprehensive numerical simulations to evaluate the structural integrity and construction feasibility of the proposed lunar building system.

In accordance with Chinese specifications for material mechanical property testing and considering practical experimental constraints, the sintering tests of simulated lunar soil were conducted using cubic specimens with 40 mm side lengths. This study systematically analyzed the specimens' post-sintering morphological characteristics and evaluated key mechanical properties, including density, elastic modulus, and shrinkage, under controlled temperature and pressure conditions. The experimental results demonstrate that specimens sintered at 1050 ℃ under pressurized conditions exhibit optimal mechanical performance, characterized by superior processing quality and enhanced mechanical stability compared to other test conditions.

Given the absence of bonding materials for *in-situ* lunar surface construction, this study adopts the self-locking structural concept of the ancient Afghan vault as a reference model. Through parametric modeling using finite element analysis software, the structural performance was evaluated by comparing deformation patterns and stress-strain distributions under both static loading and simulated moonquake conditions. Numerical simulation results indicate that the configuration with $\alpha = 30°$ and $\theta = 80°$ demonstrates optimal stability, exhibiting minimized stress and strain under identical loading conditions.

This research integrates experimental material characterization with parametric finite element analysis to optimize the lunar Afghan vault. While the current scope focuses on numerical verification, the structural feasibility is intrinsically supported by the precedent of traditional Afghan vaults, whose self-locking mechanism has been successfully validated in terrestrial construction practices. The stability and mortarless nature of this typology make it an ideal candidate for an unpressurized external shielding shell to protect lunar habitats from radiation and meteorites. By grounding the simulation in experimentally derived material properties and proven geometric typologies, this study identifies the optimal configuration. These findings establish a rigorous theoretical foundation and essential design parameters for the next phase of research. Subsequent efforts will advance toward physical fabrication and experimental validation to assess real-world construction tolerances, while further refining the characterization of frictional contact behavior between modular components.

Data availability statement

The data or datasets that support the findings of this study are available from the corresponding author upon reasonable request.

Declaration of generative AI and AI-assisted technologies

The authors did not use generative AI or AI-assisted technologies in the writing of this manuscript.

Acknowledgments

The work presented in this article was supported by the National Natural Science Foundation of China (U22B2092).

Authors' contribution

Qian Zhang: conceptualization, validation, formal analysis, writing—original draft preparation. Huifang Chen: conceptualization, data curation, writing—original draft preparation. Jingyao Zhang: formal analysis, writing—review and editing. Yao Qu: resources, visualization. SeungDeog Kim: software, project administration. Xuening Jiang: software, formal analysis, data curation. Jian Feng: methodology, supervision. Jianguo Cai: validation, resources, funding acquisition. All authors have read and agreed to the published version of the manuscript.

Conflicts of interest

Jianguo Cai holds the position of Associate Editor for *Smart Construction* and has not peer reviewed or made any editorial decisions for this paper.

References

[1] Crawford IA, Anand M, Cockell CS, Falcke H, Green DA, *et al.* Back to the moon: the scientific rationale for resuming lunar surface exploration. *Planet. Space Sci.* 2012, 74(1):3–14.

[2] Kristmann K, Raadik T, Altosaar M, Grossberg-Kuusk M, Krustok J, *et al.* Pyrite as promising monograin layer solar cell absorber material for *in-situ* solar cell fabrication on the Moon. *Acta Astronaut*. 2022, 199:420–424.

[3] Creech S, Guidi J, Elburn D. Artemis: an overview of NASA's activities to return humans to the Moon. In *Proceedings of the 2022 IEEE Aerospace Conference*, Montana, USA, March 5–12, 2022, pp. 1–7.

[4] Jianlan S. China emphasizes international cooperation in future lunar and deep space exploration. *Bull. Chin. Acad. Sci*. 2019, 2:72–79.

[5] Jones A, Patel P, Waltz E, Bajema N. The latest developments in technology, engineering, and science: news. *IEEE Spectr.* 2021, 58(10):6–13.

[6] An HJ. South Korea's space program: activities and ambitions. *Asia Policy* 2020, 15(2):34–42.

[7] Hoshino T, Wakabayashi S, Ohtake M, Karouji Y, Hayashi T, *et al.* Lunar polar exploration mission for water prospection-JAXA's current status of joint study with ISRO. *Acta Astronaut*. 2020, 176:52–58.

[8] Flahaut J, van der Bogert CH, Crawford IA, Vincent-Bonnieu S. Scientific perspectives on lunar exploration in Europe. *npj Microgravity* 2023, 9(1):50.

[9] Zhou C, Gao Y, Zhou Y, She W, Shi Y, *et al.* Properties and characteristics of regolith-based materials for extraterrestrial construction. *Engineering* 2024, 37:159–181.

[10] Liu Z, Wang Z, Cheng K, Wang C, Ha C, *et al.* Performance assessment of closed Brayton cycle-organic Rankine cycle lunar base energy system: thermodynamic analysis, multi-objective optimization. *Energy* 2023, 278:127936.

[11] Anand M, Crawford IA, Balat-Pichelin M, Abanades S, van Westrenen W, *et al.* A brief review of chemical and mineralogical resources on the Moon and likely initial *in situ* resource utilization (ISRU) applications. *Planet. Space Sci*. 2012, 74(1):42–48.
[12] Zhou C, Tang B, Ding L, Sekula P, Zhou Y, *et al.* Design and automated assembly of Planetary LEGO Brick for lunar *in-situ* construction. *Autom. Constr*. 2020, 118:103282.
[13] Wang Q, Feng P, Jansen K, Bao C. A novel rigidizable inflatable lunar habitation system: design concept and material characterization. *Mater. Des*. 2024, 246:113289.
[14] Feng Y, Pan Z, Tang X, Wang Z, Li Y, *et al.* A comprehensive review of lunar lava tube base construction and field research on a potential Earth test site. *Int. J. Min. Sci. Technol*. 2024, 34(9):1201–1216.
[15] Hurwitz DM, Head JW, Hiesinger H. Lunar sinuous rilles: distribution, characteristics, and implications for their origin. *Planet. Space Sci.* 2013, 79:1–38.
[16] Brennan L, Siecinski R, Tremayne M, Patel A, Patel P, *et al.* Mechanical design of a lunar habitat structure and deployment mechanism. *Acta Astronaut*. 2023, 213:102–120.
[17] Dronadula R, Benaroya H. Hybrid lunar inflatable structure. *Acta Astronaut*. 2021, 179:42–55.
[18] Ulubeyli S. Lunar shelter construction issues: the state-of-the-art towards 3D printing technologies. *Acta Astronaut*. 2022, 195:318–343.
[19] Benaroya H, Bernold L, Chua KM. Engineering, design and construction of lunar bases. *J. Aerosp. Eng*. 2002, 15(2):33–45.
[20] Bao C, Feng P, Zhang D, Wang Q, Yang S. Conceptual design and experimental investigation of regolith bag structures for lunar *in situ* construction. *J. Build. Eng.* 2024, 95:110245.
[21] Cohen MM. Mobile lunar base concepts. In *Proceedings of the 2004 AIP Conference on Thermophys.in Microgravity*, Albuquerque, USA, February 4, 2004, pp. 845–853.
[22] Cesaretti G, Dini E, De Kestelier X, Colla V, Pambaguian L. Building components for an outpost on the Lunar soil by means of a novel 3D printing technology. *Acta Astronaut*. 2014, 93:430–450.
[23] Yang S, Feng P, Zhang D, Zuo Y, Qi J, *et al.* Research on simulated lunar soil solar concentrator melting experiment for *in-situ* construction on lunar surface (In Chinese). *J. Huazhong Univ. Sci. Technol.* 2024, 52(8):130–138.
[24] Sumini V, Wald S, Mueller C, Chesi C, Weck OD. Multiobjective optimization for structural design of lunar habitats. In *16th Biennial International Conference on Engineering, Science, Construction, and Operations in Challenging Environments, Earth and Space 2018*, Cleveland, USA, April 9–12, 2018, pp. 169–182.
[25] Bao C, Zhang D, Wang Q, Cui Y, Feng P. Lunar *in situ* large-scale construction: quantitative evaluation of regolith solidification techniques. *Engineering* 2024, 39:204–221.
[26] Crockett RS, Fabes BD, Nakamura T, Senior CL. Construction of large lunar structures by fusion welding of sintered regolith. In *Proceedings of the 1994 International Conference on Engineering, Construction and Operations in Space*, Albuquerque, USA, February 26–March 3, 1994, pp. 1116–1127.
[27] Fateri M, Gebhardt A. Process parameters development of selective laser melting of lunar regolith for on□site manufacturing applications. *Int. J. Appl. Ceram. Technol*. 2015, 12(1):46–52.
[28] Pilehvar S, Arnhof M, Pamies R, Valentini L, Kjoniksen AL. Utilization of urea as an accessible superplasticizer on the moon for lunar geopolymer mixtures. *J. Clean. Prod*. 2020, 247:119177.

[29] Clinton RG. The road to realizing in-space manufacturing. In *Proceedings of Committee on Space-Based Additive Manufacturing of Space Hardware Meeting*, Washtington, USA, February 5–7, 2014, pp. 3251.
[30] Liao H, Zhu J, Chang S, Xue G, Pang J, *et al.* Lunar regolith-AlSi10Mg composite fabricated by selective laser melting. *Vacuum* 2021, 187:110122.
[31] Gualtieri T, Bandyopadhyay A. Compressive deformation of porous lunar regolith. *Mater. Lett*. 2015, 143:276–278.
[32] Indyk SJ, Benaroya H. A structural assessment of unrefined sintered lunar regolith simulant. *Acta Astronaut*. 2017, 140:517–536.
[33] National University of Defense Technology. GB/T 7314-2017 Metallic materials—Compression test method at room temperature. 2017. Available: https://openstd.samr.gov.cn/bzgk/std/newGbInfo?hcno=8216FA25DB28F50FD47096AB26198632 (accessed on 18 Feb 2024).
[34] Shaanxi Institute of Building Research and Design. JGJ 70-2009 Standard for test method of basic properties of construction mortar. 2009. Available: https://ebook.chinabuilding.com.cn/zbooklib/book/detail/show?SiteID=1&bookID=57890 (accessed on 18 Feb 2024).
[35] China Academy of Building Research. GB/T 50081-2019 Standard for test methods of con-crete physical and mechanical properties. 2019. Available: https://ebook.chinabuilding.com.cn/zbooklib/book/detail/show?SiteID=1&bookID=114599 (accessed on 18 Feb 2024).
[36] Xi'an Research and Design Institute of Wall &Roof Materials Co.,Ltd., China Building M-aterial Test & Certification Group Xi'an Co. Ltd. GB/T 2542-2012 Test methods for wall bricks. 2012. Available: https://openstd.samr.gov.cn/bzgk/gb/newGbInfo?hcno=A73C13F8E6EC7D9D99517971C1D69F9F (accessed on 18 Feb 2024).
[37] Ceramics Research Institute of Light Industry of China. GB/T 4740-2024 Test method for strength of ceramic materials. 2024. Available: https://openstd.samr.gov.cn/bzgk/gb/newGbInfo?hcno=D6BB5B27710005999503673127B6E607 (accessed on 18 Feb 2024).
[38] Heiken GH, Vaniman DT, French BM. *Lunar sourcebook:a user's guide to the Moon.* Cambridge: Cambridge University Press, 1991. pp. 285–356.
[39] Indyk JS, Benaroya H. A structural assessment of unrefined sintered lunar regolith simulant. *Acta Astronaut*. 2017, 140:517–536.
[40] Toklu YC, Akpinar P. Lunar soils, simulants and lunar construction materials: an overview. *Adv. Space Res*. 2022, 70(3):762–779.
[41] He X, Xiao L, Huang J, Wang C, Wu T, *et al.* Lunar soil simulant development and lunar soil simulant CUG-1A. *Geol. Sci. Technol. Inf*. 2011, 30(4):137–142.
[42] Balla VK, Roberson L, O'Connor GW, Trigwell S, Bose S, *et al.* First demonstration on direct laser fabrication of lunar regolith parts. *Rapid Prototyp. J*. 2012, 18(6):451–457.
[43] Warren P, Raju N, Ebrahimi H, Krsmanovic, M, Raghavan S, *et al.* Effect of sintering temperature on microstructure and mechanical properties of molded Martian and Lunar regolith. *Ceram. Int*. 2022, 48(23):35825–35833.
[44] Yoldas C. A prototypical (school) design strategy for soil-cement construction in Afghanistan. Doctoral Thesis, Kansas State University, 2004.
[45] Bertetto AM, Riberi F. Form-finding of pierced vaults and digital fabrication of scaled prototype. *Engineering* 2021, 8(1):210–224.

[46] Marseglia PS, Micelli F, Aiello MA. Analysis of equivalent diaphragm vault structures in masonry construction under horizontal forces. *Heritage* 2020, 3(3):989–1017.

[47] Oberst J, Nakamura Y. A seismic risk for the lunar base. In *the Second Conference on Lunar Bases and Space Activities of the 21st Century*, Houston, USA, April 5–7, 1988, pp. 231–233.